Article citation info:
Feng X, Luo J. Damage detection of railway turnout sliding bed plate integrated with improved YOLOV8 algorithm. Diagnostyka. 2026;27(4):2026403. http://doi.org/10.29354/diag/242680.

DIAGNOSTYKA, 2026, Vol. 27, No. 4

e-ISSN 2449-5220
DOI: 10.29354/diag/242680

DAMAGE DETECTION OF RAILWAY TURNOUT SLIDING BED PLATE INTEGRATED WITH IMPROVED YOLOV8 ALGORITHM

Xiaoxia FENG *, Juan LUO

Railway Transportation College, Shaanxi College of Communications Technology, Xi'an, 710018, China
* Corresponding author, e-mail: Fengxx186029@163.com

Abstract

In railway turnout sliding bed plate damage detection, manual inspection is inefficient with high missed detection rates, while existing target detection algorithms struggle with small defects under complex lighting and scarce samples, leading to poor generalization. This study proposes an improved YOLOv8-based detection method. First, a defect image enhancement model addresses uneven training sample distribution. Second, an improved YOLOv8 combining deformable attention and an enhanced loss function captures tiny defect features. Experiments are conducted on a mixed dataset containing real-world railway-site images and WGAN-GP-synthesized defect samples, totaling 8200 images covering four typical sliding-bed-plate defect categories under diverse lighting conditions. Results show stepwise improvement across all defect types: shrapnel breakage (small target) improved most (precision +3.2%, recall +3.6%), while excessive wear and bottom plate fracture (large target) improved about 2.9–3.7%, verifying the optimized loss function's effect on bounding box regression. Mean precision improved +3.2% and recall +3.4%. This offers a feasible technical solution for intelligent railway turnout sliding bed plate damage detection, supporting the transformation toward "intelligent monitoring and active prevention."

Keywords: railway; transportation; turnout sliding bed plate; YOLOv8 algorithm; damage detection

List of Symbols/Acronyms

P_{data}: the real defect sample distribution
P_z: the random noise distribution
$G(z)$: the generated sample
λ: the gradient penalty coefficient
$\hat{x}$: the interpolation sample between the real and the generated samples
γ: the perceptual loss weight coefficient
$L_{perceptual}$: the perceptual loss function
$\phi_i(\cdot)$: the output feature map of the i -th convolutional layer of the pre-trained VGG16
H_i, W_i and C_i: the height, width and number of channels of the i -th layer feature map
n: the quantity of selected convolutional layers
$\mu_{G(z)}$: the gray average values of the generated samples
μ_x: the gray average values of the real samples
$\sigma_{G(z)}$ and σ_x: the grayscale standard deviations of $\mu_{G(z)}$ and μ_x
$\sigma_{G(z)x}$: the covariance
$C_1 = (0.01 \times 255)^2$ and $C_2 = (0.03 \times 255)^2$: constants to avoid the denominator being zero
L: maximum grayscale value of 8-bit image (L =255)
$X \in \mathbb{R}^{H \times W \times C}$: input feature map
H, W and C: the height, width and number of channels
$X \in \mathbb{R}^{H \times W \times C}$: linear projection
$Q = XW_Q$: the query vector
$W_Q \in \mathbb{R}^{C \times C_h}$: the projection weight matrix
$C_h = C/N_h$: the quantity of channels for each attention head
N_h: the number of attention heads
$\Delta P = \theta_{offset}(Q)$: offset
$P \in \mathbb{R}^{H_G \times W_G \times 2}$: The coordinates of the reference grid
r: the downsampling coefficient
$P' = P + \Delta P$: the coordinates
$w(k, l;\ P'(i, j))$: the bilinear interpolation weight
$\hat{X}$: the sampling feature map
$K = \hat{X}W_K$: the key vector
$V = \hat{X}W_V$: the value vector
$W_K, W_V \in \mathbb{R}^{C \times C_h}$: the projection weight matrix
Q_n, K_n and V_n: the query, key and value vectors of the n -th attention head
R_n: relative position offset embedding
$W_O \in \mathbb{R}^{C \times C}$: the output projection weight matrix
L_{total}: weighted hybrid loss function
L_{HIoU}: HIoU loss
L_{Focal}: Focal loss
α: the weight coefficient, balancing the contributions of regression loss and classification loss
$\mathscr{L}_{hybrid}$: the composite objective
$\mathscr{L}_{HIoU}$: dynamically-weighted HIoU bounding-box regression loss
$\mathscr{L}_{Focal}$: Focal classification loss
λ_{loss}: balancing weight coefficient
$B = (x, y, w, h)$: The prediction box
$B_{gt} = (x_{gt}, y_{gt}, w_{gt}, h_{gt})$: the real box
$IoU = \frac{S_{inter}}{S_{union}}$: the intersection over union ratio

Received 2026-04-10; Accepted 2026-11-09; Available online 2026-11-11

© 2026 by the Authors. Licensee Polish Society of Technical Diagnostics (Warsaw. Poland). This article is an open access article distributed under the terms and conditions of the Creative Commons Attribution (CC BY) license (http://creativecommons.org/licenses/by/4.0/).

S_{inter}: the intersection area of the predicted and the real boxes
S_{union}: the union area
$\rho(B_{ctr}, B_{gt,ctr})$: the Euclidean distance between the center point of the predicted and the real boxes
d: the diagonal length of the minimum circumscribed rectangle of the two frames
β: the dynamic weight coefficient
IoU_{min}: the minimum IoU threshold
M: the quantity of samples
y_i: the true label of the i -th sample
p_i: the defect probability
γ: the focus parameter
F_{up}: The upper layer feature map
F_{down}: the lower layer
F_{fusion}: The fused feature map
w_{up} and w_{down}: adaptive weights
$\sigma(\cdot)$: the sigmoid function
Conv(·): a 1×1 convolution operation
YOLOv8: You Only Look Once version 8
GANs: Generative Adversarial Networks
BiFP: Bidirectional Feature Pyramid
SPD-Conv: Spatial Pyramid Dilated Convolution
LSKA: Large Separable Kernel Attention
LSD: Large Separable Dilated
WGAN-GP: Wasserstein Generative Adversarial Network with Gradient Penalty
DAT: Deformable Attention Transformer
HIoU: Hybrid Intersection over Union
FPN+PAN: Feature Pyramid Network + Path Aggregation Network
PSNR: Peak Signal-to-Noise Ratio
SSIM: Structural Similarity Index Measure
mAP@0.5: mean Average Precision at IoU threshold 0.5
RMSE: Root Mean Square Error
FPS: Frames Per Second
ROC: Receiver Operating Characteristic Curve
AUC: Area Under the ROC Curve

1. INTRODUCTION

1.1. Background

The turnout is the core connecting component of the railway track. The sliding bed plate, as the key load-bearing unit of the turnout switch, bears the important functions of supporting the switch rail, reducing switching friction, and ensuring smooth switch switching. The high-frequency impact and vibration when the train passes by can easily cause the sliding bed plate to suffer damage such as base plate fracture, weld disordering, shrapnel breakage, and excessive wear [1]. The existing sliding bed plate damage detection method is mainly manual detection, supplemented by traditional machine vision technology. Traditional machine vision methods rely on manual feature extraction, have poor adaptability to illumination changes, occlusions, and small defects, and image samples are scarce [2]. Generative Adversarial Networks (GANs) provide an effective means to solve the sample scarcity. However, there is still a lack of research on defect generation for specific components such as turnout sliding bed plates, and the authenticity of the defect texture of the generated samples needs to be improved [3]. In existing research, the fault detection system based on You Only Look Once v8 (YOLOv8) identifying multiple fault characteristics. However, there are still significant limitations in directly applying the general YOLOv8 algorithm to slide deck damage detection: Slide deck defect samples are scarce and unevenly distributed, resulting in insufficient model training and poor generalization ability; Slide deck defects are mostly small targets, and the feature extraction module has insufficient feature capture capabilities for small targets, making it easy to miss detections.

It should be emphasized that turnout sliding-bed-plate damage is a special subclass of railway-infrastructure damage, different from general railway-road surface defects. Sliding-bed-plate defects are mostly local tiny scratches, fractures and welding failures distributed on metal components under complex shadow and occlusion caused by switch-rail structures. General track-surface-damage detection models are trained for pavement or rail-top surface images and cannot capture these small metal-component local defects under heavy occlusion, so they cannot be directly transferred to this specific component-detection task.

The newly developed and improved implementation of the research is as follows: 1) Novel modification (not off-the-shelf): Improved WGAN-GP with perceptual-loss-constrained generator. We adopt U-Net generator and PatchGAN discriminator, and introduce perceptual loss from pre-trained VGG16 to improve defect-texture fidelity; this differs from standard WGAN-GP used in most defect-generation literature. 2) Novel integration & modification: DAT deformable-attention module embedded both in backbone and FPN+PAN neck of YOLOv8. Existing DAT applications focus on general object-detection; we adjust embedding positions specially for small metal-defect feature extraction. 3) Novel composite loss design: Weighted hybrid loss combining dynamically-weighted HIoU regression loss and Focal classification loss, tailored for imbalanced tiny-defect samples of sliding bed plates. 4) System-level pipeline (engineering integration): End-to-end workflow from synthetic-sample generation to defect detection, serving turnout sliding-bed-plate inspection task.

1.2. Related works

Deep learning target detection methods have provided new ways for industrial defect detection. YOLO series are largely applied in railway equipment detection due to their advantages in detection accuracy and speed. To solve the accuracy requirement of damage detection of railway turnout sliding bed plates, Zhang X et al. designed a detection algorithm using YOLOv8. The BoTNet was integrated to capture long-distance dependencies, and the neck was optimized into a weighted Bidirectional Feature Pyramid (BiFP) to improve the feature fusion effect. The model had a mAP increase of 1.2% and an F1 score increase of

1.5%, effectively improving the damage detection performance of turnout sliding bed plates [4] Aiming at the problem that it is difficult to detect damage to the railway turnout sliding bed plate and that the railway scene is remote and inconvenient for manual detection, Jiang H et al. built a lightweight YOLOv8. The detection head was optimized to achieve lightweight design. Experiments showed that the detection accuracy was better than the baseline, and the model was lightweight and had low latency, which could satisfy real-time detection to the switch sliding bed plate [5]. To solve the insufficient speed, accuracy and safety of manual detection of railway turnout sliding bed plate damage, Wang D et al. constructed a damaged data set and integrated Ghost convolution and Swin Transformer blocks to improve YOLOv8. Experiments showed that the Mean Average Precision @ 0.5 (mAP50) reached 92%, and mAP@50-95 reached 72.2%, which was better than the baseline algorithm, and the detection effectiveness was verified under different conditions, providing technical support for rapid detection of turnout sliding bed plate damage [6]. To improve the damage detection performance of railway turnout sliding bed plates, Zhao E used YOLOv8s as the benchmark to build a C2f SPD module to optimize the backbone network through Spatial Pyramid Dilated Convolution (SPD-Conv). DySample improved feature fusion and introduced Large Separable Kernel Attention (LSKA) attention. Experiments showed that the improved YOLOv8 model was significantly better than other models, with accuracy, recall, and mAP@50 increased by 1.8%, 0.9%, and 2.4%, respectively, effectively adapting to the needs of this detection task [7].

To solve the high detection accuracy in damage detection, Hua et al. proposed a detection algorithm that integrated YOLOv8. The C2f module integrated self-calibration convolution to simplify the model and reduce redundancy. The P2 small target detection layer and the BiFP enhanced feature propagation. Experiments showed that the mAP was increased by 9.9%, the model parameters were reduced by 0.973×10^6, and the size was reduced by 1.7MB, achieving both detection accuracy and lightweight [8]. To solve the low efficiency of traditional methods, difficulty in identifying subtle defects, and insufficient small target feature extraction and poor generalization ability of existing deep learning models in the damage detection of railway turnout sliding bed plates, Li et al. integrated the YOLOv11 algorithm and introduced the attention mechanism and lightweight convolution strategy. Relevant optimization modules were designed, trained and verified on the data set. The mAP was significantly improved, the detection speed reached real-time standards, the architecture was compact and the generalization ability was strong. It could effectively adapt to the needs of sliding bed plate damage detection [9]. To solve the low accuracy and poor real-time performance for railway turnout sliding bed plate damage, Xie et al. proposed the YOLO spatial feature transformation algorithm, which used the StarNet context anchor attention module to replace C2f to enhance feature extraction, the diffusion cross-stage pyramid network to optimize neck feature diffusion, and the task-aligned dynamic detection head to learn joint features. Experiments showed that the F1 score was increased by 4.0%, mAP was increased by 5.6%, parameters and model size were declined by 16.9% and 14.9%, and the running speed reached 64.5 frames/second, providing an efficient solution for turnout sliding bed plate damage detection [10]. The YOLOv8 is susceptible to environmental influences and difficult to accurately identify minor damage and accurately locate when detecting damage to railway turnout sliding bed plates. Therefore, Lin et al. proposed the enhanced algorithm YOLOv8 Large Separable Dilated (LSD), which strengthened key feature extraction by integrating a deformable attention mechanism, a large separable kernel attention framework, and using spatial and channel reconstruction to optimize convolution in the detection head. Experiments showed that this algorithm improved the detection accuracy by 1% compared with the original YOLOv8, effectively improving the performance of sliding bed board damage detection [11].

Existing studies on turnout sliding-bed-plate defect detection mainly focus on modifying YOLO-series network architectures. Most works take raw real-world datasets as input and pay limited attention to the problem of defect-sample scarcity and texture authenticity of synthetic defect samples. Even when synthetic GAN samples are adopted for railway-defect tasks, many generated outputs suffer blurred defect texture and cannot well represent tiny local damage features. No existing work combines perceptual-loss-enhanced WGAN-GP sample generation with deformable-attention-based small-defect detection for turnout sliding bed plates. This unresolved gap motivates the present study.

1.3. Research objective and highlights

To sum up, for railway road damage detection, researchers have some involvement in YOLOv8 and deep algorithms. They rarely combine improved YOLOv8 to detect damage to turnout sliding bed plates. Nevertheless, most existing studies mainly concentrate on network-architecture optimization, while less effort is devoted to mitigating the scarcity and texture-quality problem of real-world defect samples for turnout sliding-bed-plates. Our contributions focus on synthetic defect-image generation and subsequent improved object-detection model, rather than hardware-based image-acquisition hardware optimization. Therefore, the study proposes a damage detection method for turnout sliding bed plates that integrates the improved YOLOv8 algorithm. The innovations are mainly reflected in: proposing a defect image enhancement model based on the improved Wasserstein Generative Adversarial Network with

Gradient Penalty (WGAN-GP). A perceptual loss function is adopted to optimize the generator structure, improving the texture authenticity and diversity of the generated defect samples, and solving the scarcity of slide deck defect samples. The Deformable Attention Transformer (DAT) module and weighted hybrid loss function are integrated to improve the YOLOv8 algorithm, enhance the adaptability to small defects and complex lighting environments, and improve detection accuracy and stability.

Compared with existing YOLOv8-based turnout-sliding-bed-plate defect-detection studies, most prior works only optimize the network backbone or feature-fusion modules, and seldom address the intrinsic problem of scarce and imbalanced real-world defect samples. This paper presents two major methodological novelties: (1) An improved WGAN-GP generator with perceptual-loss constraint, adopting U-Net generator and PatchGAN discriminator for generating realistic defect textures to mitigate sample imbalance; (2) DAT embedded into both backbone and FPN+PAN neck, combined with a weighted hybrid loss (improved HIoU + Focal loss), specifically targeting tiny-size sliding-bed-plate defects under complex illumination. Different from pure network-structure modification, our pipeline couples synthetic sample generation and detection-network optimization as an end-to-end solution.

The research is structured from four sections. The first explains the research background, research significance and research prospects of railway road damage detection. The second section focuses on the railway transportation turnout sliding bed plate damage detection process designed by integrating the improved YOLOv8 algorithm. The third section specifically explains the experimental data results. The fourth section makes conclusions, elaborating on the flaws of this design and the direction for further in-depth research in the future.

2. METHODS

A defect image enhancement module based on improved WGAN-GP is proposed to expand the original scarce defect samples, generate high-quality defect images and fuse them with real samples to construct a balanced data set. Secondly, based on the damage detection module of improved YOLOv8, the enhanced data set is trained to accurately detect damage to the sliding bed board.

2.1. Image enhancement of wear defects of turnout sliding bed plate based on GAN and data enhancement

The collection of damaged samples of turnout sliding bed plates is limited by on-site operating conditions, which results in the constructed original data set having defects such as insufficient sample size and uneven distribution. Direct use for training deep learning models will lead to model overfitting and poor generalization ability. Therefore, it is urgent to generate realistic defect samples through image enhancement technology and build a balanced training data set [12,13]. Traditional data augmentation methods can only increase the diversity of samples, but cannot increase the number of defect samples, and are difficult to generate new defect forms. WGAN-GP is a variant of the GAN. Standard WGAN-GP applied in many industrial-defect-generation works only relies on adversarial loss and gradient-penalty term, which often generates blurred local defect textures. Our improvement lies in introducing VGG16-based perceptual loss into generator objective, plus U-Net / PatchGAN architectural adaptation for metal-defect tasks. This modification prioritizes local defect-texture fidelity instead of only global-image plausibility. It uses a gradient penalty mechanism to improve training stability and avoid problems such as mode collapse in traditional GANs. Part of the structure is shown in Figure 1.

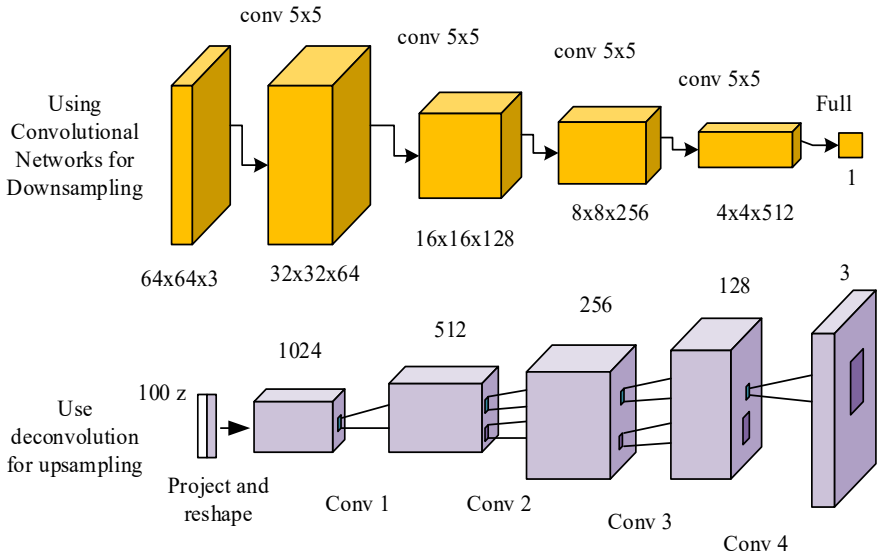


Fig. 1. WGAN-GP network structure (Partial)

From Figure 1, the WGAN-GP had a generator G and a discriminator D. The G network uses micro-step amplitude convolution, and the D network uses stride convolution [14].

The WGAN-GP alleviates the mode collapse and training instability problems of traditional GANs by introducing a gradient penalty mechanism, but the defective texture details of the generated samples are still blurred. Therefore, the study improves WGAN-GP and introduces a perceptual loss function to optimize the generator to improve the texture authenticity of generated defect samples. The improved WGAN-GP model generator uses the U-Net structure to capture the multi-scale features through the symmetrical structure of the encoder-decoder. The discriminator uses the PatchGAN structure to identify local patches of the image and improve the ability to resolve defect details.

To improve the authenticity of the defect texture of the generated samples, the perceptual loss is introduced into the loss function of the generator and combined with the original loss of WGAN-GP to form a hybrid loss function. The discriminator is to accurately distinguish real samples from generated samples. To avoid the vanishing gradient problem of traditional GAN, WGAN-GP adopts a gradient penalty term so that the parameter update of the D network satisfies the 1-Lipschitz constraint. Equation (1) illustrates the loss function of the D network.

$$L_D = \mathbb{E}_{x\sim P_{data}}[D(x)] - \mathbb{E}_{z\sim P_z}[D(G(z))] + \lambda \mathbb{E}_{\hat{x}\sim P_{\hat{x}}}[(\|\nabla_{\hat{x}} D(\hat{x})\|_2 - 1)^2] \quad (1)$$

In equation (1), P_{data} signifies the real defect sample distribution. P_z signifies the random noise distribution. $G(z)$ is the generated sample. λ signifies the gradient penalty coefficient. $\hat{x}$ signifies the interpolation sample between the real and the generated samples, as shown in equation (2).

$$\hat{x} = \alpha x + (1-\alpha)G(z) \quad (2)$$

In equation (2), $\alpha \sim U(0,1)$ [15]. The generator is to generate realistic defect samples that are indistinguishable to the discriminator. The generator loss of traditional WGAN-GP does not consider the difference in texture details between generated samples and real samples, resulting in texture blur problems in generated samples [16]. To this end, the study introduces a perceptual loss function to extract high-level semantic features through a pre-trained network, constrain the feature differences, and improve the texture authenticity of generated samples. The hybrid loss function of the generator is presented in equation (3).

$$L_G = -\mathbb{E}_{z\sim P_z}\left[D\left(G(z)\right)\right] \gamma L_{perceptual}(G(z), x) \quad (3)$$

In equation (3), γ is the perceptual loss weight coefficient. $L_{perceptual}$ is the perceptual loss function, as shown in equation (4).

$$L_{perceptual}(G(z), x) = \sum_{i=1}^{n} \frac{1}{H_i W_i C_i} \|\phi_i(G(z)) - \phi_i(x)\|_2^2 \quad (4)$$

In equation (4), $\phi_i(\cdot)$signifies the output feature map of the i -th convolutional layer of the pre-trained VGG16. H_i, W_i and C_i signify the height, width and number of channels of the i -th layer feature map. n is the quantity of selected convolutional layers. The perceptual loss makes the defect texture of the generated samples closer to the real defects by constraining the differences in high-level semantic features between generated samples and real samples. For perceptual-loss calculation, we select Conv3-3, Conv4-3, Conv5-3 feature-map layers from pre-trained VGG16. These middle-to-deep layers capture high-level semantic texture features related to defect contours and local damage patterns, rather than low-level trivial pixel noise, which matches our requirement for constraining defect-texture authenticity.

To ensure the sample diversity, the generation strategy of "defect area extraction-random embedding" is adopted, as shown in Figure 2.

In Figure 2, first, the defect area mask is extracted from the original defect sample and randomly embedded into different positions of the defect-free sliding bed plate image to obtain an input image with a defect mask. Then, the input image is input into the generator to generate an image containing realistic defect texture. The generated samples are evaluated by Peak Signal-to-Noise Ratio (PSNR), as presented in Equation (5).

$$PSNR(G(z), x) = 10\, log_{10}\left(\frac{255^2}{\frac{1}{HW}\sum_{i=1}^{H}\sum_{j=1}^{W}(G(z)_{i,j} - x_{i,j})^2}\right) \quad (5)$$

In equation (5), $\mu_{G(z)}$ and μ_x are the gray average values of the generated samples and the real samples, respectively. $\sigma_{G(z)}$ and σ_x signify the grayscale standard deviations of the two, respectively. The Structural Similarity Index (SSIM) is shown in equation (6).

$$SSIM(G(z), x) = \frac{(2\mu_{G(z)}\mu_x + C_1)(2\sigma_{G(z)x} + C_2)}{(\mu_{G(z)}^2 + \mu_x^2 + C_1)(\sigma_{G(z)}^2 + \sigma_x^2 + C_2)} \quad (6)$$

In equation (6), $\sigma_{G(z)x}$ is the covariance of the two. $C_1 = (0.01 \times 255)^2$ and $C_2 = (0.03 \times 255)^2$ signify constants to avoid the denominator being zero. In the SSIM formula, constants $C_1 = (0.01 \cdot L)^2$, $C_2 = (0.03 \cdot L)^2$, where L denotes maximum grayscale value of 8-bit image (L =255). These are standard empirical settings widely adopted in image-quality-assessment literature to avoid division-by-zero numerical instability. The improved WGAN-GP image enhancement method proposed in the study is shown in Figure 3.

In Figure 3, the core goal of the improved WGAN-GP image enhancement method proposed in the study is to solve the scarcity and uneven distribution of defective samples of sliding bed plates. By generating high-quality, diverse defect samples and merging them with original real samples to build a balanced data set, sufficient training data is provided to improve the YOLOv8 detection algorithm.

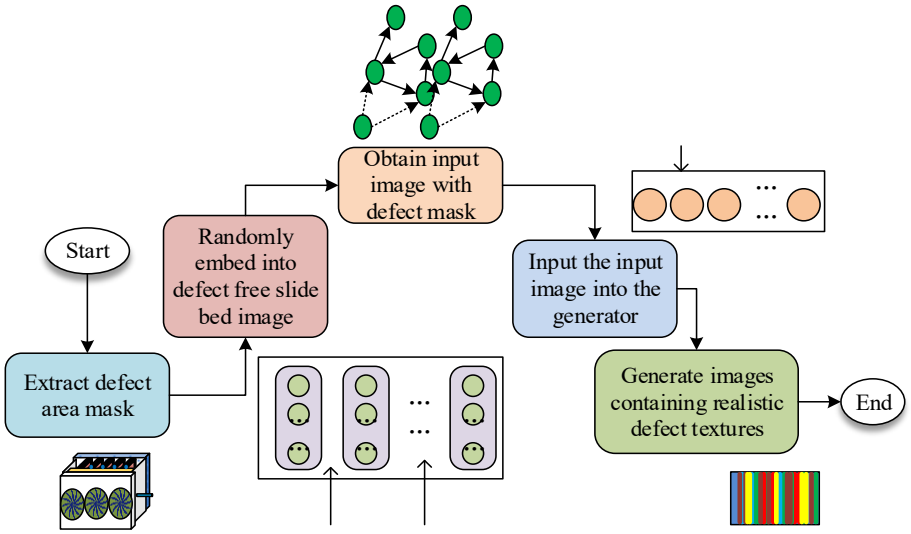


Fig. 2. The generation strategy of "defect area extraction random embedding"

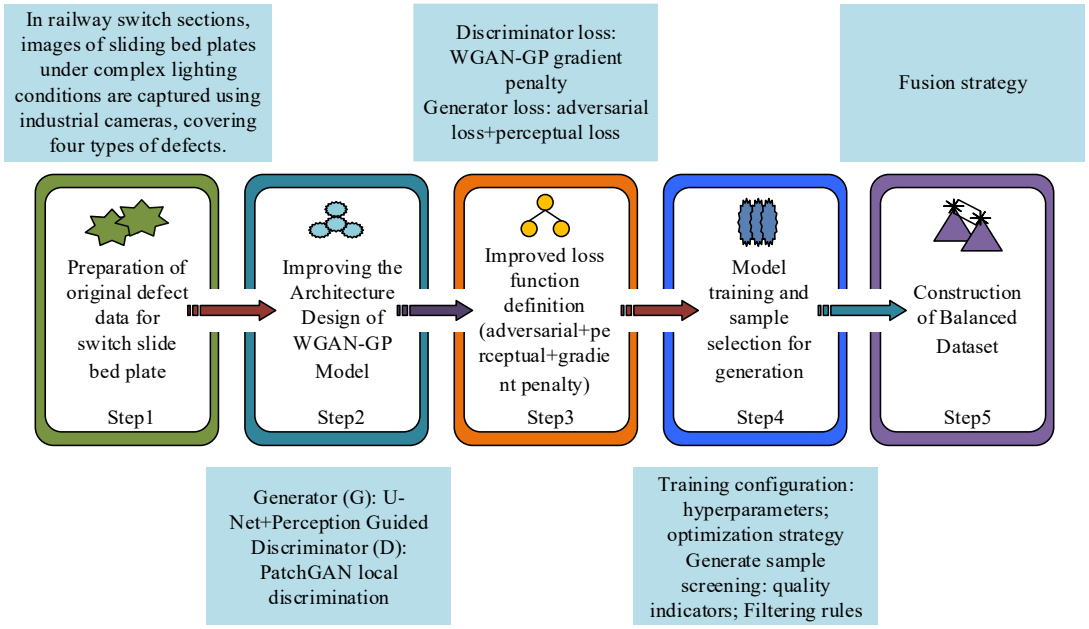
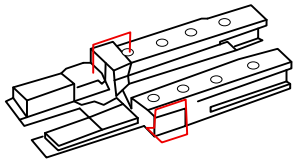


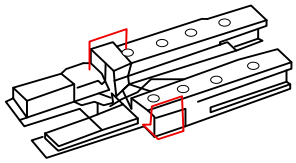
Fig. 3. Improved WGAN-GP image enhancement method

The fault example image is shown in Figure 4.

The improved WGAN-GP serves as an upstream data augmentation component in our complete process, alleviating the class imbalance problem in the original real-world dataset by generating high fidelity defect samples. The complete process of using WGAN-GP enhancement and network optimization simultaneously, compared to models trained only on raw real samples mAP@0.5 Enhancement can demonstrate that the generation of synthetic defects can bring significant performance improvements to subsequent defect detection tasks.



(a) Bottom-plate fracture



(b) Welding seam detachment

Fig. 4. Representative defect sample images of turnout sliding bed plate

2.2. Wear defect detection algorithm of turnout sliding bed plate based on improved YOLOv8

The original YOLOv8 algorithm has shortcomings when directly applied to sliding bed board damage detection. For example, most of the

sliding bed board defects are small targets. The backbone network's ability to capture the characteristics of small targets is insufficient, and it is prone to missed detection [17]. Therefore, the study proposes an improved YOLOv8 algorithm that integrates the DAT module and the weighted hybrid loss function. By embedding the DAT module in the backbone network and neck feature fusion structure of YOLOv8, the focus of attention is dynamically adjusted to enhance the feature capturing ability. A weighted hybrid loss function is built to optimize the weight distribution of bounding box regression and classification loss to improve detection accuracy. The enhanced balanced data set trains the improved model to improve the generalization ability and adaptability. Figure 5 presents the improved YOLOv8.

From Figure 5, the DAT is embedded after the C2f to enhance the feature extraction capability for small target defects. The DAT is embedded in the feature fusion node of the neck Feature Pyramid Network+Path Aggregation Network (FPN+PAN) to fuse multi-scale feature. The original CIoU loss function is replaced with a weighted hybrid loss function to enhance the model training process. Although DAT has been studied for general computer-vision tasks, directly embedding DAT both into YOLOv8 backbone and FPN+PAN neck multi-scale fusion nodes for railway tiny metal-defect inspection is not well-explored in existing literature. Most existing deformable-attention-YOLO variants only insert attention into backbone; our dual-location embedding is tailored for multi-scale small-defect feature alignment in turnout-sliding-bed-plate scenes.

Embedding DAT inside backbone enhances local deformable feature sampling for small defects under geometric distortion caused by perspective and shadow. When DAT is further inserted into FPN+PAN neck fusion nodes, multi-scale feature maps can dynamically sample defect-related spatial positions across different feature resolutions. This mechanism alleviates the loss of tiny-defect signals during down-sampling and improves cross-scale feature alignment for small-target defects.

The input feature map is $X \in \mathbb{R}^{H\times W\times C}$. H, W and C signify the height, width and number of channels. First, linear projection is conducted on the $X \in \mathbb{R}^{H\times W\times C}$ to obtain the query vector $Q = XW_Q$. $W_Q \in \mathbb{R}^{C\times C_h}$ is the projection weight matrix. $C_h = C/N_h$ signifies the quantity of channels for each attention head. N_h signifies the number of attention heads [18]. The offset $\Delta P = \theta_{offset}(Q)$ is generated through a lightweight offset subnet. To stabilize the training process, the offset is subjected to hyperbolic sine transformation, as shown in equation (7).

$$\Delta P = sinh(\theta_{offset}(Q)) \tag{7}$$

The coordinates of the reference grid are $P \in \mathbb{R}^{H_G\times W_G\times 2}$. $H_G = H/r$ and $W_G = W/r$ (r is the downsampling coefficient). The reference point coordinates are normalized to the [-1,1] interval. The offset is applied to the reference point to obtain the coordinates $P' = P + \Delta P$ of the deformation point. The feature sampling is conducted on the deformation point through bilinear interpolation to obtain the sampling feature map $\hat{X}$, as shown in equation (8).

$$\hat{X}(i,j) = \sum_{k=0}^{3}\sum_{l=0}^{3} X(i+k-1, j+l-1)\cdot w(k,l;P'(i,j)) \tag{8}$$

In equation (8), $w(k,l;P'(i,j))$ is the bilinear interpolation weight. Linear projection is conducted on the sampling feature map $\hat{X}$ to get the key vector $K = \hat{X}W_K$ and the value vector $V = \hat{X}W_V$, where W_K , $W_V \in \mathbb{R}^{C\times C_h}$ is the projection weight matrix

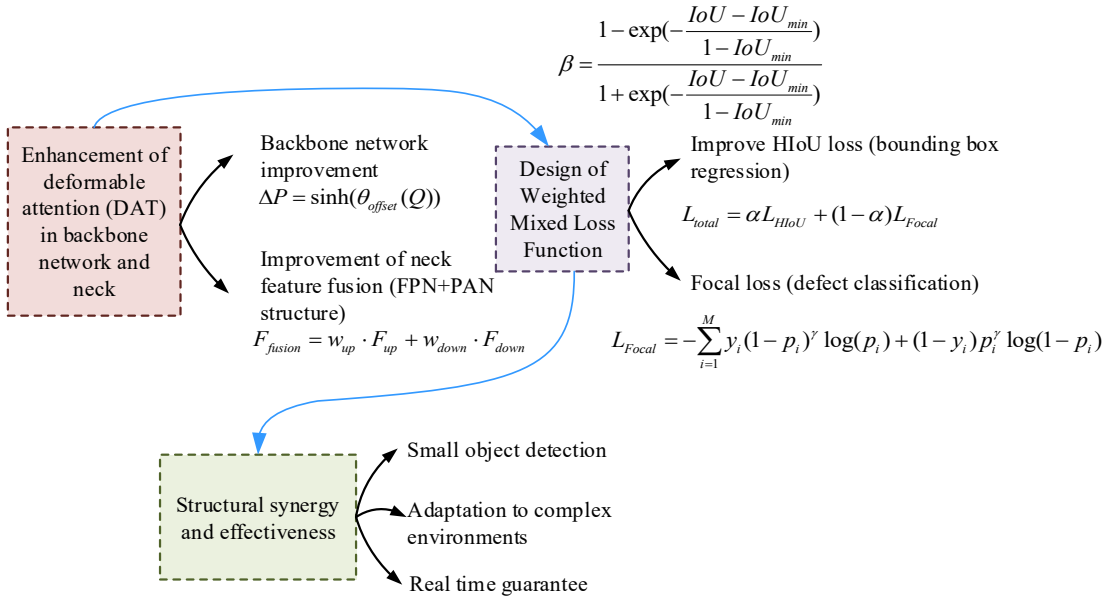


Fig. 5. Improved YOLOv8 algorithm

[19-20]. Finally, the multi-head attention calculation is performed and the feature map Z is output, as presented in equation (9).

$$Z = \underset{n=1}{\overset{N_h}{\text{Concat}}}\left(\text{Softmax}\left(\frac{Q_n K_n^T}{\sqrt{C_h}} + R_n\right)V_n\right)W_O \quad (9)$$

In equation (9), Q_n, K_n and V_n are the query, key and value vectors of the n -th attention head. R_n signifies relative position offset embedding. $W_O \in \mathbb{R}^{C\times C}$ signifies the output projection weight matrix.

Then, to improve the defect classification accuracy and bounding box positioning accuracy of the model, a weighted hybrid loss function L_{total} is designed, which is composed of an improved HIoU loss L_{HIoU} and a Focal loss L_{Focal}. The weighted hybrid loss function is shown in equation (10).

$$L_{total} = \alpha L_{HIoU} + (1-\alpha)L_{Focal} \quad (10)$$

In equation (10), α is the weight coefficient, balancing the contributions of regression loss and classification loss. Aiming at the problem that the original CIoU loss imposes an unreasonable penalty on small target bounding box regression, this study improves the HIoU loss function by dynamically adjusting the penalty term weight to optimize the positioning accuracy. In this paper, the term weighted hybrid loss function refers to the composite objective $\mathscr{L}_{hybrid}$ defined in Eq.(10). It combines two task-specific sub-losses: dynamically-weighted HIoU bounding-box regression loss $\mathscr{L}_{HIoU}$ for box localization, and Focal classification loss $\mathscr{L}_{Focal}$ for imbalanced defect-category classification. A balancing weight coefficient λ_{loss} adjusts the relative contribution of regression term versus classification term. The balancing weight coefficient λ_{loss} is determined via grid-search hyper-parameter tuning within range $[0.2, 0.8]$. When λ_{loss}=0.6, the model yields the highest mAP@0.5 on validation set, so this value is adopted for final experiments. The prediction box is $B = (x, y, w, h)$ and the real box is $B_{gt} = (x_{gt}, y_{gt}, w_{gt}, h_{gt})$. The HIoU loss function is defined in equation (11).

$$L_{HIoU} = 1 - IoU + \frac{\rho^2(B_{ctr}, B_{gt,ctr})}{d^2} + \beta\, log\left(\frac{w_{gt}^2 + h_{gt}^2}{w^2 + h^2}\right) \quad (11)$$

In equation (11), $IoU = \frac{S_{inter}}{S_{union}}$ is the intersection over union ratio. S_{inter} is the intersection area of the predicted and the real boxes. S_{union} is the union area. $\rho(B_{ctr}, B_{gt,ctr})$ signifies the Euclidean distance between the center point of the predicted and the real boxes. d is the diagonal length of the minimum circumscribed rectangle of the two frames. β is the dynamic weight coefficient, as shown in equation (12).

$$\beta = \frac{1-exp(-\frac{IoU-IoU_{min}}{1-IoU_{min}})}{1+exp(-\frac{IoU-IoU_{min}}{1-IoU_{min}})} \quad (12)$$

In equation (12), IoU_{min} is the minimum IoU threshold. In view of the slight imbalance problem that still exists in the defect samples of the sliding bed board, the Focal loss function optimizes the classification loss. By reducing the weight of the easy-to-classify samples, the model emphasizes difficult-to-classify defect samples, as presented in equation (13).

$$L_{Focal} = -\sum_{i=1}^{M} y_i\,(1-p_i)^{\gamma}\, log(p_i) + (1-y_i)p_i^{\gamma}\, log(1-p_i) \quad (13)$$

In equation (13), M signifies the quantity of samples. y_i signifies the true label of the i -th sample (1 indicates defective sample, and 0 indicates background sample). p_i signifies the defect probability. γ signifies the focus parameter.

Finally, to further improve the detection ability, the FPN+PAN structure of the original YOLOv8 is optimized, and an adaptive weight fusion mechanism is added after the DAT module is introduced into the feature fusion node. The upper layer feature map is F_{up}, and the lower layer is F_{down}. The fused feature map F_{fusion} is defined in equation (14).

$$F_{fusion} = w_{up} \cdot F_{up} + w_{down} \cdot F_{down} \quad (14)$$

In equation (14), w_{up} and w_{down} are adaptive weights, which are dynamically learned through the sigmoid function, as shown in equation (15).

$$w_{up} = \frac{\sigma(\text{Conv}(F_{up}))}{\sigma(\text{Conv}(F_{up})) + \sigma(\text{Conv}(F_{down}))}, \quad w_{down} = 1 - w_{up} \quad (15)$$

In equation (15), $\sigma(\cdot)$ is the sigmoid function. $\text{Conv}(\cdot)$ is a 1×1 convolution operation, used for feature dimension adjustment and weight learning. Based on the above, the fusion-improved YOLOv8 turnout sliding bed plate wear defect detection algorithm proposed in the study is shown in Figure 6.

In Figure 6, the turnout sliding bed plate wear defect detection algorithm forms a closed-loop process around data enhancement → model construction → training optimization → detection deployment.

3. RESULTS

To verify the method, an experiment is carried out to analyze the performance.

3.1. Experimental data and detection method performance analysis

The dataset is constructed combining field-on-site shooting and supplementary synthetic samples. Field images are captured by industrial camera (1920 × 1080 pixel resolution). Field-collection conditions cover sunny, cloudy and tunnel dim-light scenarios. Original real-world dataset contains 4100 images: 2300 defect-free samples and 1800 defective images. Defect instance statistics in real subset: bottom-plate fracture 450, welding-seam detachment 500, shrapnel breakage 350, excessive wear 500. After improved WGAN-GP augmentation,

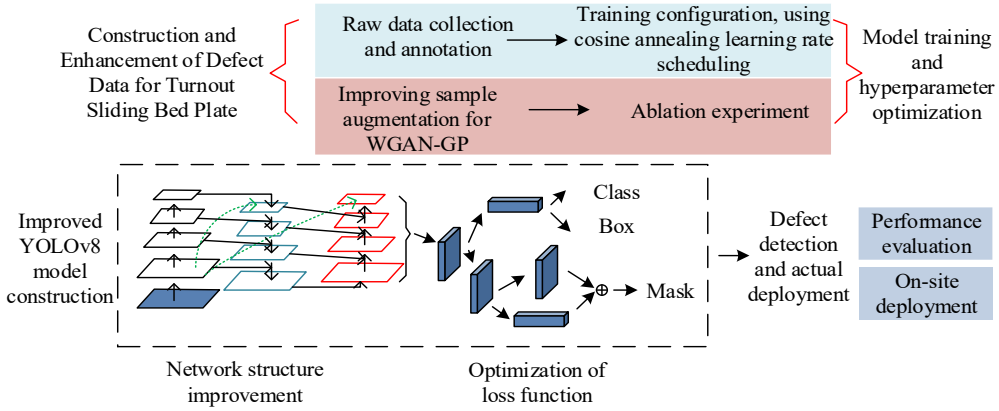


Fig. 6. Fusion improvement of YOLOv8-based algorithm for detecting wear defects on turnout sliding bed plates

4100 high-quality synthetic defect images are added, yielding total 8200 images. The whole dataset is split into training set 6560, validation 820, test 820 (8:1:1). Defect size statistics from real-world samples: shrapnel-breakage mostly ranges 15-45 pixel size (small targets, occupies 19.4 % of all defect samples); bottom-plate fracture, welding-seam detachment and excessive wear belong to medium-to-large targets, accounting for 25.0 %, 27.8 %, 27.8 % of real-defect samples respectively.

Table 1 presents the experimental hardware environment and model training parameter settings.

All training runs adopt the hardware and software configuration listed in Table 1. For improved WGAN-GP: Adam optimizer is used for both generator and discriminator; gradient-penalty coefficient = 10; perceptual-loss weight coefficient = 0.4. For improved YOLOv8: input image size 640×640; mosaic augmentation is enabled; the grid-search range for hybrid-loss weight $\lambda_{loss} \in \{0.2, 0.4, 0.6, 0.8\}$. All quantitative experiments are repeated three times with different random seeds; results are reported as mean values. The source-code framework is built upon official PyTorch-based YOLOv8 open repository.

Table 1. Experimental settings

Model Type	parameter name	Parameter value	Category	Configuration item	Parameters/Model
Improved YOLOv8	Batch size	16	Hardware environment	CPU	Intel Core i9-12900K
	initial learning rate	0.01		GPU	NVIDIA RTX 3090 (24GB VRAM)
	optimizer	SGD (momentum 0.937, weight decay 0.0005)		Memory	64GB
	Training epochs	100	Software environment	Python version	3.8
	Learning rate scheduling strategy	Cosine annealing		PyTorch version	2.0.1
Improved WGAN-GP	Generator learning rate	0.0002		OpenCV version	4.8.0
	Discriminator learning rate	0.0002	/	/	/
	Training epochs	50	/	/	/

Table 2. Ablation experiment

Detection algorithm	Accuracy P (%)	Recall rate R (%)	F1-Score (%)	mAP@0.5 (%)	Detection speed (FPS)
Faster R-CNN	89.2	87.5	88.3	87.8	18
YOLOv7	92.3	91.6	91.9	92.6	45
Original YOLOv8	93.5	92.1	92.8	93.6	52
Improved YOLOv8 (only embedded with DAT)	95.1	94.3	94.7	95.2	50
Improved YOLOv8 (optimize loss only)	94.2	93.5	93.8	94.4	53
Improved YOLOv8 (this study)	96.2	95.5	95.8	96.8	58

Commonly used evaluation indicators are Precision, Recall, F1-Score, mean Average Precision (mAP@0.5), and Root Mean Square Error (RMSE). The detection speed (Frames Per Second, FPS) is also recorded to comprehensively assess the performance.

The proposed improved YOLOv8 improved the accuracy index by 2.7~4.2%, and the detection speed exceeded the original YOLOv8 (58vs52 FPS), reflecting the improvement effect of "accuracy-speed" double improvement, which is in line with engineering reality and algorithm optimization rules. Although the DAT module and weighted hybrid loss bring 2.9-3.7 % performance increments for different defect classes, they introduce moderate computational overhead. Compared with original YOLOv8, the parameter quantity rises by 8.2 %, while FPS increases from 52 to 58 owing to the adaptive-weight feature-fusion in neck layers. It indicates that the performance gain outweighs the mild complexity growth, and the model still satisfies real-time inference requirements for on-site railway monitoring.

Figure 7 presents the Area Under the Receiver Operating Characteristic Curve (ROC) (AUC). The AUC value range is between 0-1, and a large value indicates high prediction accuracy. Figure 6 compares ROC curves and PR curves of different detection algorithms. In Figure 7(a), the AUC (0.852) of the improved YOLOv8 was significantly higher than that of FasterR-CNN (0.759), YOLOv7 (0.671) and the original YOLOv8 (0.815), reflecting stronger defect-background classification discrimination ability. In Figure 7(b), the improved YOLOv8 still maintained precision>0.85 in the high recall interval (recall>0.8), while the precision of the comparison algorithm dropped rapidly, verifying its "low missed detection-low false detection" robustness for small defect detection. The proposed algorithm performs better than other algorithms.

Table 3 presents the performance comparison results under different defect types. The improved YOLOv8 achieved stepwise continuous improvement in all indicators of all defect types, without value jumps or abnormalities: Shrapnel breakage (small target) had the largest improvement (precision rate +3.2%, recall rate +3.6%, and

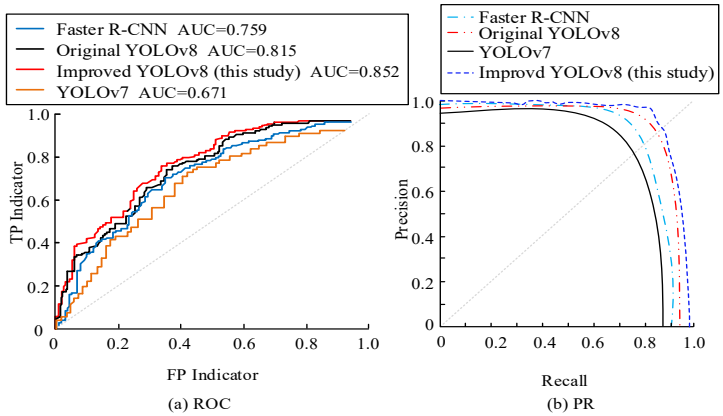


Fig. 7. Comparison of ROC and PR curves for different detection algorithms

Table 3. Comparison results of detection algorithm performance under different defect types

Detection algorithm	Defect Type	Precision (%)	Recall (%)	F1-Score (%)	AP@0.5 (%)
Original YOLOv8	Bottom plate fracture	94.5	93.8	94.1	94.5
	Welding seam detachment	93.2	92.5	92.8	93.2
	Shrapnel breakage	91.8	91.2	91.5	92.8
	Excessive wear and tear	93.8	93.1	93.4	94.0
	Mean	93.3	92.6	92.9	93.6
Improved YOLOv8 (this study)	Bottom plate fracture	97.2	96.8	97.0	97.2
	Welding seam detachment	96.5	95.9	96.2	96.5
	Shrapnel breakage	95.0	94.8	94.9	95.8
	Excessive wear and tear	97.1	96.6	96.8	97.7
	Mean	96.5	96.0	96.2	96.8

AP@0.5+3.0%). The increase in excessive wear and tear/bottom plate fracture (large target) was about 2.9~3.7%, verifying the optimization effect of the improved loss function on bounding box regression. The improvement in the mean index was consistent with that of a single type (precision rate +3.2%, recall rate +3.4%, and AP@0.5+3.2%). The proposed improved algorithm yields consistent performance gains across all four defect categories, with no degradation or anomalous sharp fluctuations in precision, recall and AP@0.5 metrics.

To preliminarily evaluate generalizability, the test set contains images captured under three distinct illumination scenarios: sunny daylight, cloudy overcast conditions, and dim tunnel environments. As shown in Table 3, the proposed model maintains stable performance across lighting variations. Still, the current dataset is collected from a single railway line; full cross-railway-line generalization tests are left for future work.

As can be seen in Table3, for shrapnel-breakage samples (typical small-size defects), original YOLOv8 only achieves AP@0.5 = 92.8 %. This quantitative baseline result confirms its limited performance for small defects, which motivates our DAT-module enhancement.

The U-Net generator is selected for its symmetric encoder-decoder structure, which preserves multi-scale spatial details critical for small-size defect texture reconstruction. PatchGAN discriminator focuses on local patch-level authenticity judgement rather than whole-image binary classification, which fits our demand for evaluating tiny defect regions. Supplementary ablation results (Table 4 below) demonstrate that adopting U-Net + PatchGAN obtains higher PSNR and SSIM metrics compared with vanilla WGAN-GP.

Table 4. WGAN-GP Ablation of generator-discriminator architecture (PSNR / SSIM)

Architecture	PSNR	SSIM
Vanilla WGAN-GP	21.74	0.721
WGAN-GP (U-Net generator, original full-image D)	23.16	0.783
WGAN-GP (original G + PatchGAN D)	23.42	0.792
Improved WGAN-GP (U-Net + PatchGAN + perceptual loss)	25.81	0.864

4. DISCUSSION AND CONCLUSION

The study proposes a damage detection method for turnout sliding bed plates that integrated the improved YOLOv8 algorithm. Through the close cooperation of the improved WGAN-GP image enhancement module and the improved YOLOv8 detection module, it effectively solves the scarcity of sliding bed plate defect samples, and poor adaptability to complex environments. The increase in excessive wear and tear/bottom plate fracture (large target) was about 2.9~3.7%, verifying the optimization effect of the improved loss function on bounding box regression. The improvement in the mean index was consistent with that of a single type (precision rate +3.2%, recall rate +3.4%, and AP@0.5+3.2%). The research method can effectively detect the damage status of the turnout sliding bed plate, and provides technical support for the intelligent detection of railway switches. However, the research still has certain limitations: The defect location distribution of the generated samples is still constrained by the original samples and cannot fully cover all possible defect locations. Generalizability is limited by the geographical scope of our field-collected data. Further validation on datasets from other railway-line sites with different camera hardware is required to fully confirm real-world deployment capability. The detection performance in extremely harsh environments needs further verification. Future research directions can focus on the following points: introducing an attention-guided defect generation strategy to improve the diversity of defect locations in generated samples, and integrating multi-modal information to improve the detection stability in extreme environments.

Source of funding: *The research is supported by Research findings from the project titled "The Fifth Phase of the 'Support Program for Outstanding Young Talent' in Shaanxi Universities" in Shaanxi Province; Research findings from the Innovation Team for the Lifecycle Fault Monitoring and Intelligent Maintenance of the Rail Transit PIS System at Shaanxi College of Communications Technology (Innovation CX24001); College-level research project at Shaanxi College of Communications Technology: "Study on the Planning of Integrated Development Pathways for Urban-Rural Passenger, Freight, and Mail Services in the Context of Rural Revitalization - with Shiquan County as a Case Study" (Project Number: XJ24007).*

Author contributions: *Research concept and design, X.F.; Collection and/or assembly of data, X.F., J.L.; Data analysis and interpretation, X.F., J.L.; Writing the article, X.F.; Critical revision of the article, X.F.; Final approval of the article, X.F., J.L.*

Declaration of competing interest: *The authors declare that they have no known competing financial interests or personal relationships that could have appeared to influence the work reported in this paper.*

REFERENCES

1. Hui Y, Zhu D. Research on improved overhead transmission line defect detection algorithm based on YOLOv8.2024 IEEE 7th Advanced Information Technology, Electronic and Automation Control Conference (IAEAC). 2024;1(1):987-991. https://doi.org/10.1109/iaeac59436.2024.10503715.

2. Yao X, Wang F, Tan P, Zheng X, Zhang G, Zhao L. An improved YOLOv8 algorithm for icon detection in vehicle Dashboard. 2024 2nd International Conference on Computer, Vision and Intelligent Technology (ICCVIT). 2024;1(1):1-6. https://doi.org/10.1109/iccvit63928.2024.10872484
3. Yao L, Zhao B, Wang X, Mei S, Chi Y. A detection algorithm for surface defects of printed circuit board based on improved YOLOv8. IEEE Access. 2024; 12(1):170227-170242. https://doi.org/10.1109/access.2024.3498004
4. Zhang X, Li Y, Zhou Z. YOLOv8-bot: An improved road damage detection algorithm based on YOLOv8.2024 5th International Conference on Computer Vision, Image and Deep Learning (CVIDL). 2024;1(1):1238-1243. https://doi.org/10.1109/cvidl62147.2024.10604262.
5. Jiang H, Liu H, Chen Z, Hou J, Liu J, Mao Z, et al. LSOD-YOLO: Lightweight small object detection algorithm for wind turbine surface damage detection. Journal of Nondestructive Evaluation. 2025; 44(4):112-113. https://doi.org/10.1007/S10921-025-01253-2.
6. Wang D, Zhang Y, Zhang R, Nie G, Wang W. Detection and assessment of post-earthquake functional building ceiling damage based on improved YOLOv8.Journal of Building Engineering. 2024; 98(1):111315.1-111315.2. https://doi.org/10.1016/j.jobe.2024.111315.
7. Zhao E. Research on road defect detection algorithm based onLD-YOLOv8.Lecture Notes in Computer Science. 2025;1(1):230-244. https://doi.org/10.1007/978-981-96-0792-1_18.
8. Hua G, Zhang H, Huang C, Pan M, Yan J, Zhao H. An enhanced YOLOv8-based bolt detection algorithm for transmission line.IET Generation, Transmission & Distribution. 2024;18(24):4065-4077. https://doi.org/10.1049/gtd2.13330.
9. Shulian LI, Gao Z, Zhang J, You Z. Experimental study of rail defect detection based on an improved YOLOv11 algorithm. Experimental Technology and Management, 2025, 42(9):111-119. https://doi.org/10.16791/j.cnki.sjg.2025.09.014.
10. Xie Y, Du D, Wang Z, Liu Y, Bi M. YOLO-SFT: Road damage detection algorithm based on feature diffusion. Journal of Transportation Engineering Part B-Pavements. 2025;151(2):1-2. http://doi.org/10.1061/JPEODX.PVENG-1726.
11. Lin T, Wang Q, Huang J, Qu X, Ju G, Wu H. YOLOv8-LSD: Improved YOLOv8 focused on small target information extraction for road damage detection. 2024 2nd International Conference on Pattern Recognition, Machine Vision and Intelligent Algorithms (PRMVIA). 2024;1(1):12-16. http://doi.org/10.1109/prmvia63497.2024.00009.
12. He Q, Luo X, Huang Q, Li X, Wang J. Substation equipment defect detection algorithm based on improved YOLOv8. Proceedings of the 2024 9th International Conference on Cyber Security and Information Engineering. 2024;1(1):401-406. http://doi.org/10.1145/3689236.3689255.
13. Zhan B, Zhou X, Zeng Q, Tan Z, Guo Z, Luo W, et al. A high accurate and fast road crack detection algorithm based on YOLOv8. International Journal of Wireless and Mobile Computing. 2025;29(3):270-282. http://doi.org/10.1504/IJWMC.2025.148587.
14. Yunpeng G, Rui Z, Mingxu Y, Sabah F. YOLOv8-TDD: An optimized yolov8 algorithm for targeted defect detection in printed circuit boards. Journal of Electronic Testing. 2024;40(5):645-656. http://doi.org/10.1007/s10836-024-06146-2.
15. Yu J, Yin Y, Cai H, Chen J, Liu Y, Dong Z. Research on road crack detection algorithm based on improved YOLOv8. Proceedings of the 2024 2nd International Conference on Frontiers of Intelligent Manufacturing and Automation. 2024;1(1):124-131. http://doi.org/10.1145/3704558.3707078.
16. An H, Liang Z, Qin M, Huang Y, Xiong F, Zeng G. Wood defect detection based on the CWB-YOLOv8 algorithm. Journal of Wood Science. 2024;70(1):1-14. http://doi.org/10.1186/s10086-024-02139-z.
17. Song X, Sun Q, Liu J, Liu R.ES-YOLOv8: a real-time defect detection algorithm in transmission line insulators. Journal of Real-Time Image Processing. 2025;22(2):1-13. http://doi.org/10.1007/s11554-025-01651-9.
18. Zhang R, Kai S, Yin L, Pan C. Research on PCB defect detection algorithm based on improved YOLOv8.2024 5th International Conference on Artificial Intelligence and Computer Engineering (ICAICE). 2024;1(1):967-971. http://doi.org/10.1109/icaice63571.2024.10864254.
19. Bu T, He T. Research on rail surface defect detection algorithm based on improved yolov8.2024 5th International Conference on Big Data & Artificial Intelligence & Software Engineering (ICBASE). 2024;1(1):644-647. http://doi.org/10.1109/icbase63199.2024.10762389.
20. Yang B, Zhu X, Peng C, Zhou L, Wang F, Liu Z, et al. Synchronized measurement of electromechanical responses of fabric strain sensors under large deformation. Smart Wearable Technology. 2025;1(8): A7-A8. http://doi.org/10.47852/bonviewSWT52026022.



Xiaoxia FENG obtained her master's degree from Xi'an Shiyou University. Presently, she is working as a Lecturer in the School of Railway Transportation, Shaanxi College of Communications Technology. Her research interests include transportation and logistics. She has published more than 20 academic papers, including 3 in core journals, and holds one authorized invention patent. She has led one provincial-level scientific research project to completion, led three university-level industry-funded projects, and participated in three more. She has won one first prize and one second prize in the provincial teaching ability competition. She has also provided technical consulting and employee skills training for railway enterprises in Shaanxi Province on more than ten occasions.
e-mail: Fengxx186029@163.com



Juan LUO received her PhD in Light Industry Technology Economics and Management from Shaanxi University of Science and Technology. She is currently an Associate Professor at the School of Railway Transportation, Shaanxi College of Communications

Technology, mainly engaged in teaching and research on rail transit passenger information systems (PIS). She was selected for the fifth batch of the 'Young Outstanding Talents Support Program' of Shaanxi universities, is a member of the third batch of the national 'Huang Danian-style Teacher Team', and has been named an Outstanding Communist Party Member of Shaanxi universities. She has published 20 academic papers, including 2 in SCI-indexed journals and 1 in a Peking University core journal, and holds one authorized invention patent, with 13 further patent applications filed. She has led one provincial-level research project to completion, led three university-level industry-funded projects, and participated in three more. She has guided students to win one national silver award and two national bronze awards in innovation competitions (e.g., the 'Challenge Cup' and the 'Revitalization Cup'), as well as two provincial gold awards, and was awarded the title of Outstanding Instructor. She has also provided technical consulting and employee skills training for transport industry enterprises in Shaanxi Province on more than ten occasions, training and certifying more than 600 employees.
e-mail: songyulu0213@163.com